OPEN ACCESS

Journal of Statistical Mechanics: Theory and Experiment
An IOP and SISSA journal

PAPER: Classical statistical mechanics, equilibrium and non-equilibrium

Numerical accuracy of the derivative-expansion-based functional renormalization group

Andrzej Chlebicki

Institute of Theoretical Physics, Faculty of Physics, University of Warsaw,
Pasteura 5, 02-093 Warsaw, Poland
E-mail: chlebickiandrzej@gmail.com

Received 1 August 2024
Accepted for publication 1 August 2024
Published 17 September 2024

Online at stacks.iop.org/JSTAT/2024/093204
https://doi.org/10.1088/1742-5468/ad6c31

Abstract. We investigate the precision of the numerical implementation of the functional renormalization group based on extracting the eigenvalues from the linearized renormalization group transformation. For this purpose, we implement the local potential approximation and $O(\partial^2)$ orders of the derivative expansion for the three-dimensional $O(N)$ models with $N \in \{1,2,3\}$. We identify several categories of numerical error and devise simple tests to track their magnitude as functions of numerical parameters. Our numerical schemes converge properly and are characterized by errors of several orders of magnitude smaller than the error bars of the derivative expansion for these models. We highlight situations in which our methods cease to converge, most often due to rounding errors. In particular, we observe an impaired convergence of the discretization scheme when the $\tilde{\rho}$ grid is cut off at the value $\tilde{\rho}_{\mathrm{Max}}$ smaller than 3.5 times the local potential minimum. The program performing the numerical calculations for this study is shared as an open-source library accessible for review and reuse.

Keywords: functional renormalization group, derivative expansion, numerical methods

Contents

1. Introduction

Over the past 30 years, the functional renormalization group (fRG) scheme based on the Morris–Wetterich (MW) equation has proven an efficient and versatile tool for investigating phenomena involving physics at various length scales. It was applied in a wide range of fields ranging from statistical and condensed-matter physics to gravity and high-energy physics. The success of this approach is connected to the development of well-controlled approximation schemes not relying on perturbative expansions, such as the derivative expansion (DE) [1–3]. The nonperturbative nature of this scheme, however, comes at a significant cost. The renormalization group (RG) flow equations, obtained with this approximation, take the form of nonlinear partial differential equations that seldom can be solved analytically. Consequently, most recent studies employing the DE in the MW approach rely on numerical calculations.

In recent years, significant attention has been directed towards forming a foundational understanding of the DE. The major developments include the first estimation of the convergence parameter [4], a method for calculating error bars [5], and a new rationale for choosing the infrared regulator based on the principle of maximal conformity [6]. These developments are part of a concerted effort to elevate the status of the DE to a reliable tool delivering well-controlled qualitative predictions. In this spirit, we find it paramount to investigate how the numerical errors and the choice of numerical methods affect the results of DE calculations.

The fRG literature tends to omit numerical methods. Especially in older articles, there are few references to techniques or details of numerical implementation and numerical results are often treated as exact. Nowadays, the situation is improving and more information is being provided. Still, however, only a few papers present all the information necessary to reproduce the numerical results faithfully. The lack of transparency concerning numerical implementation might be hindering the development of our methodology.

Recently, numerical methods, in the fRG context, have seen more attention. For example, [7–13] implement new integration techniques for the fRG flows in various physical contexts. These works, however, focused exclusively on the RG-flow integration. In the present work, we investigate a method of extracting critical exponents based on linearized fRG flow around a fixed point (FP), which is a subject of far fewer developments, e.g. [14, 15]. More specifically, we implement and evaluate the numerical errors of the stability-matrix approach based on the finite-grid representation of the functions parametrizing the effective average action and extracting the RG eigenvalues from the spectrum of the operator describing the linearized flow.

The purpose of the present paper is threefold. Firstly, we aim to evaluate some of the numerical methods often employed in calculations based on the DE and present simple tests that may be used to examine their reliability. Secondly, we identify several sources of numerical error in calculations of this type and show how numerical parameters can be tuned to maximize precision. Finally, the program used to perform all the calculations for the purpose of this study is shared for review in the form of a simple *Mathematica* [16] library that can be relatively easily adapted for other purposes. Our analysis is conducted in the paradigmatic $O(N)$ models in three dimensions at the local potential approximation (LPA) and $O(\partial^2)$ orders of the DE.

The structure of the paper is as follows. In section 2, we introduce the MW approach to the fRG and the approximation scheme of the DE. Section 3 is devoted to the discussion of numerical techniques used in our calculations. In section 4, we present our results regarding the convergence rates and error propagation observed in our calculations. Finally, in section 5 we discuss our results and state our conclusions.

2. fRG

In the present chapter, we offer a brief overview of the MW formulation of the fRG and the DE. For a more detailed description of this methodology and a review of its wide applications, see [17–20].

The MW approach to the fRG is centered around a scale-dependent functional of the order-parameter $\boldsymbol{\phi}$ called the effective average action Γ_k. The effective average action is defined in such a way that it smoothly interpolates between the microscopic action in the ultraviolet limit and the Gibbs free energy in the infrared (IR) limit. The flow of the effective average action is governed by the exact functional differential equation called the MW equation

$$k\partial_k\Gamma_k = \frac{1}{2}\mathrm{Tr}\left(k\partial_k R_k\right)\left(R_k + \Gamma^{(2)}\right)^{-1}. \tag{1}$$

In the equation above, R_k denotes the IR regulator function, $\Gamma^{(2)}$ is the IR-cutoff two-point function, and the trace is taken over all internal indices.

In the fRG literature, we can find several commonly used IR regulator functions R_k. In this work, we employ just two regulators:

- the Litim regulator $R_k^{\mathrm{Litim}}(\boldsymbol{q}^2) = Z^k k^2(1-\frac{\boldsymbol{q}^2}{k^2})\Theta(1-\frac{\boldsymbol{q}^2}{k^2})$,
- the exponential regulator $R_k^{\mathrm{Exp}}(\boldsymbol{q}^2) = \alpha Z^k k^2 \exp(-\frac{\boldsymbol{q}^2}{k^2})$.

In the definitions above, Θ stands for the Heaviside step function, Z^k denotes the order-parameter-renormalization factor (to be defined shortly), and α is an arbitrary positive constant. We employ the Litim regulator at the LPA level whenever we want to perform the integrals analytically and the exponential regulator otherwise. In calculations of physical quantities, the regulator constant α should be optimized via the *principle of minimal sensitivity* or the *principle of maximal conformity* to reduce the regulator dependence [6, 21]. In this work, however, we are only interested in the numerical error which can be assumed to be mostly independent of the value of α. For this reason, we refrain from optimizing the regulator and assume the value $\alpha = 1$.

The MW equation (1) is not directly soluble. The DE is an approximate scheme that recasts the MW equation into a set of partial differential equations that can be solved using numerical methods. This approximation is based on an observation that, from the perspective of long-range physics, we are mostly interested in the low-momentum region of the correlation function. We, therefore, expand the effective average action in powers of the order-paramater's momentum around a spatially homogeneous order-parameter configuration.

In practice, the DE is set up by imposing an ansatz on the effective average action Γ_k. A proper DE ansatz at the order $O(\partial^p)$ contains all terms respecting the required symmetries of up to pth power of the spatial-derivative operator. In the present work, we consider the $O(N)$-symmetric theories of an N-component scalar field. The leading- and next-to-leading-order DE ansätze for these models read:

$$\Gamma_k^{\mathrm{LPA}} = \int \mathrm{d}^d x \left\{U^k(\rho) + \frac{1}{2}\left(\partial_\mu\phi^i\right)^2\right\}, \tag{2a}$$

$$\Gamma_k^{\partial^2} = \int \mathrm{d}^d x \left\{U^k(\rho) + \frac{Z_\pi^k(\rho)}{2}\left(\partial_\mu\phi^i\right)^2 + \frac{Z_\sigma^k(\rho) - Z_\pi^k(\rho)}{4\rho}\left(\partial_\mu\rho\right)^2\right\}, \tag{2b}$$

where the parametrizing functions U^k, Z^k_σ, and Z^k_π depend on the order parameter $\boldsymbol{\phi}$ only through the $O(N)$ invariant $\rho = \frac{\phi^i \phi^i}{2}$. In such a parametrization, all the symmetry constraints are fulfilled by construction. To preserve the analyticity of the action, however, we have to impose an additional constraint $Z^k_\sigma(0) = Z^k_\pi(0)$. At the leading order, called the LPA, the effective action is parametrized by just one function $U^k(\rho)$—the local potential. The order $O(\partial^2)$ introduces two kinetic coefficients $Z^k_\sigma(\rho)$ and $Z^k_\pi(\rho)$ [1]. Many studies also employ the so-called LPA' truncation, which is an intermediate step between LPA and $O(\partial^2)$ orders of the DE. In this truncation, the kinetic terms are reduced to flowing constants $Z^k_\sigma(\rho) = Z^k_\sigma$, $Z^k_\pi(\rho) = Z^k_\pi$, or to a single flowing constant $Z^k_\sigma = Z^k_\pi = Z^k$. The DE was successfully applied to the $O(N)$ models up to the order $O(\partial^4)$ for generic values of N and up to the order $O(\partial^6)$ for $N = 1$[4, 5].

We derive the flow equations by plugging the effective action ansätze into the MW equation (1). The flow of the local potential is derived by evaluating equation (1) in a spatially uniform field configuration

$$\phi^i_{\boldsymbol{q}} = \phi\,\delta_{i,1}\delta_{\boldsymbol{q},0}, \tag{3}$$

while the flow of kinetic coefficients is extracted from the flow of $\Gamma^{(2)}$ vertices via:

$$\beta^k_U(\rho) = k\partial_k U^k(\rho) = k\partial_k \Gamma_k[\boldsymbol{\phi}]\big|_{\text{Uniform}}, \tag{4a}$$

$$\beta^k_{Z_\sigma}(\rho) = k\partial_k Z^k_\sigma(\rho) = \frac{1}{2d}\Delta_{\boldsymbol{p}}\left(k\partial_k \Gamma^{(2)}_{k;1\boldsymbol{p},1-\boldsymbol{p}}\right)\Big|_{\text{Uniform, }\boldsymbol{p}=0}, \tag{4b}$$

$$\beta^k_{Z_\pi}(\rho) = k\partial_k Z^k_\pi(\rho) = \frac{1}{2d}\Delta_{\boldsymbol{p}}\left(k\partial_k \Gamma^{(2)}_{k;2\boldsymbol{p},2-\boldsymbol{p}}\right)\Big|_{\text{Uniform, }\boldsymbol{p}=0}. \tag{4c}$$

The β functions defined in equation (4) do not depend on the local potential directly, only through its derivatives. It is, therefore, convenient to reframe the problem in terms of $V^k(\rho) = \partial_\rho U^k(\rho)$. The β function for the derivative of the local potential reads:

$$\beta^k_V(\rho) = -\frac{1}{2}\int \frac{\mathrm{d}^d\boldsymbol{q}}{(2\pi)^d}\left[k\partial_k R_k\left(\boldsymbol{q}^2\right)\right]\left\{\frac{3V'(\rho) + 2\rho V''(\rho) + \boldsymbol{q}^2 Z'_\sigma(\rho)}{\left[V(\rho) + 2\rho V'(\rho) + Z_\sigma(\rho)\,\boldsymbol{q}^2 + R_k\left(\boldsymbol{q}^2\right)\right]^2}\right.$$
$$\left. + (N-1)\frac{V'(\rho) + \boldsymbol{q}^2 Z'_\pi(\rho)}{\left[V(\rho) + Z_\pi(\rho)\,\boldsymbol{q}^2 + R_k\left(\boldsymbol{q}^2\right)\right]^2}\right\}, \tag{5}$$

where the scale k indices were suppressed for clarity. We refrain from presenting the β functions for the kinetic coefficients, as they are quite lengthy. They are presented in the online repository serving as an appendix to this article [22].

---

[1] In the Ising universality class [$N = 1$], the kinetic terms $(\partial_\mu \phi^1)^2$ and $(\partial_\mu \rho)^2 = 2\rho(\partial_\mu \phi^1)^2$ are proportional. The ansatz (2b) is constructed in such a way that, for $N = 1$, $Z^k_\pi(\rho)$ drops out of the ansatz and loses its physical significance. Consequently, there remain just two physically relevant independent parametrizing functions $U^k(\rho)$, $Z^k_\sigma(\rho)$. In the calculations of the present work, we perform the calculations for the $O(1)$ model including the nonphysical operators connected to $Z^k_\pi(\rho)$. This choice does not affect the physical eigenvalues except for numerical errors.

In the present work, we investigate the linearized RG flow around a FP solution. To make the fixed-point behavior manifest we express the equations in terms of dimensionless variables by performing the following rescaling:[2]

$$\begin{aligned} \tilde{\rho} &= \rho k^{2-d} Z^k, & \tilde{V}^t(\tilde{\rho}) &= V^k(\rho)\, k^{-2} Z^{k^{-1}}, & \tilde{Z}^t_{\sigma/\pi}(\tilde{\rho}) &= Z^k_{\sigma/\pi}(\rho)\, Z^{k^{-1}}, \\ t &= -\log(k/\Lambda), & \tilde{\beta}_V(\tilde{\rho}) &= \beta^k_V(\rho)\, k^{-2} Z^{k^{-1}}, & \tilde{\beta}_{Z_{\sigma/\pi}}(\tilde{\rho}) &= \beta^k_{Z_{\sigma/\pi}}(\rho)\, Z^{k^{-1}}. \end{aligned} \tag{6}$$

The order-parameter-renormalization factor Z^k, used in the rescaling, is defined by normalizing one of the dimensionless kinetic factors [typically $\tilde{Z}_\pi$] to unity at an arbitrary point $\tilde{\rho}_\eta$

$$\tilde{Z}^t_\pi(\tilde{\rho}_\eta) = Z^k_\pi(\rho_\eta)/Z^k \equiv 1. \tag{7}$$

In the present work, we choose $\rho_\eta = 0$, which conveniently removes the choice between normalizing $\tilde{Z}_\sigma$ and $\tilde{Z}_\pi$ since $Z^k_\sigma(0) = Z^k_\pi(0)$. We also define the *running anomalous dimension* η_t, serving as a precursor to the fixed-point anomalous dimension η^*, as the logarithmic derivative of the order-parameter-renormalization factor $\eta_t = \partial_t \log(Z^k)$.

In terms of the dimensionless variables, the flow equations take the form:

$$\partial_t \tilde{V}(\tilde{\rho}) = (\eta_t - 2)\tilde{V}(\tilde{\rho}) - (d - 2 + \eta_t)\tilde{\rho}\tilde{V}'(\tilde{\rho}) - \tilde{\beta}_V(\tilde{\rho}), \tag{8a}$$

$$\partial_t \tilde{Z}_\sigma(\tilde{\rho}) = \eta_t \tilde{Z}_\sigma(\tilde{\rho}) - (d - 2 + \eta_t)\tilde{\rho}\tilde{Z}'_\sigma(\tilde{\rho}) - \tilde{\beta}_{Z_\sigma}(\tilde{\rho}), \tag{8b}$$

$$\partial_t \tilde{Z}_\pi(\tilde{\rho}) = \eta_t \tilde{Z}_\pi(\tilde{\rho}) - (d - 2 + \eta_t)\tilde{\rho}\tilde{Z}'_\pi(\tilde{\rho}) - \tilde{\beta}_{Z_\pi}(\tilde{\rho}), \tag{8c}$$

in which the explicit renormalization-time t dependence has been removed. In the form (8), the flow equations can be used to find the FP solutions

$$\partial_t \mathcal{F}^* = \partial_t \begin{pmatrix} \tilde{V}^* \\ \tilde{Z}^*_\sigma \\ \tilde{Z}^*_\pi \end{pmatrix} = 0. \tag{9}$$

Once the FP solution $\mathcal{F}^*$ has been identified, the flow equations can be linearized to determine the RG eigenvalues which can be used to calculate the critical exponents. The linearization is performed by perturbing the FP solution:

$$\mathcal{F}_\epsilon = \mathcal{F}^* + \epsilon \begin{pmatrix} f_V \\ f_{Z_\sigma} \\ f_{Z_\pi} \end{pmatrix}, \tag{10}$$

---

[2] We note, that in the present convention the *renormalization time* t flows in the positive direction from 0 to $+\infty$, with the scale k decreasing from Λ to 0.

with $f_{Z_\pi}(t,\tilde{\rho}_\eta)=0$ and $f_{Z_\pi}(t,\tilde{\rho}=0)=f_{Z_\sigma}(t,\tilde{\rho}=0)$. The perturbed FP action (10) is inserted into the flow equations (8), which are subsequently truncated at the linear order in ϵ. After simplification, the resulting equations take the linear form:

$$\partial_t \begin{pmatrix} f_V(t,\tilde{\rho}) \\ f_{Z_\sigma}(t,\tilde{\rho}) \\ f_{Z_\pi}(t,\tilde{\rho}) \end{pmatrix} = \mathcal{M}(\tilde{\rho}) \begin{pmatrix} f_V(t,\tilde{\rho}) \\ f_{Z_\sigma}(t,\tilde{\rho}) \\ f_{Z_\pi}(t,\tilde{\rho}) \end{pmatrix}, \tag{11}$$

where $\mathcal{M}$ is a differential operator to which we shall refer as the stability operator (or stability matrix in a discretized form).

The stability operator $\mathcal{M}$ is an unbounded and asymmetrical differential operator. To our knowledge, $\mathcal{M}$ has not been comprehensively investigated from the perspective of functional analysis. Despite its incomplete mathematical understanding, the stability operator has proven to be an effective tool for calculating critical exponents. Its eigenvalues $\{e_i\}$ represent the scaling dimensions of their associated eigenoperators (or eigenvectors) F_i. When the investigated FP is critical, the leading and only positive eigenvalue of $\mathcal{M}$ is an inverse of the correlation length exponent $e_1=\nu^{-1}$, while the remaining eigenvalues, in principle, determine the correction-to-scaling exponents $\omega_i=|e_{i+1}|$.

It should be noted that not all of the eigenvalues e_i affect the scaling behavior of physical observables. Some of the eigenvectors F_i, known as the redundant operators, are connected to a reparametrization of the effective action Γ and are therefore an artifact of the employed scheme. This observation forms a basis of the so-called essential scheme of the DE [23]. In this approach, the redundant operators associated with nonlinear transformations of the order parameter are removed from the parametrization of the effective action. As a result, the spectrum of the linear RG operator calculated in the essential scheme does not include these redundant operators. From the perspective of numerical accuracy, however, the distinction between essential and redundant operators does not seem meaningful. We, therefore, implement the simpler ‘standard’ scheme and do not discuss whether the calculated eigenvalues are redundant.

3. Numerical methods

The fRG fixed-point equations (FPEs) form a set of ordinary differential equations. In the literature, we can find several different approaches to solving them numerically. One of the techniques found in the literature is the so-called shooting method (SM), in which the FPEs are integrated as an initial value problem.

The SM aims to answer the question of how to specify the initial condition corresponding to a specific global fixed-point solution. Locally, almost any initial condition leads to a local solution of the FPEs . However, only a discrete number of initial conditions lead to physically relevant global solutions [24, 25]. The SM is an iterative scheme in which the initial value problem is solved for many different initial conditions. With each iteration, the initial condition is systematically improved until the obtained solution of the FPEs specific lies closer to the global FP solution than a given tolerance threshold. After identifying the FP solution, the RG eigenvalues can be identified using the SM to solve the eigenvalue equation:

$$\mathcal{M}(\tilde{\rho})\,F_i(\tilde{\rho}) = \lambda_i\,F_i(\tilde{\rho}) \qquad (12)$$

for the stability operator $\mathcal{M}$ (see equation (11)). For more details on how this method can be implemented, see [15, 25].

The SM was used for studying the critical and multicritical behavior of the $O(N)$ models. In the Ising universality class $[N=1]$ this method was applied at the LPA order, where the initial condition is specified by a single variable, and at the $O(\partial^2)$ order, where the initial condition consists of two variables [24, 26, 27]. Similarly, for the generic value of N the SM was used at the LPA level (single-variable initial condition) and at the LPA' level (two-variable initial condition) [15, 28–31]. Curiously, we are unaware of any study implementing the SM at higher orders. This is probably due to the rapidly rising number of dimensions in the space of initial conditions. We finally note that although the intuitive approach is to integrate the FPEs from $\tilde{\rho}=0$ towards $\tilde{\rho}\to\infty$ it is not the only possible solution. Tan *et al* [15] identifies the asymptotic boundary condition at $\tilde{\rho}\to\infty$ and implements the SM integrating the FPEs from some large value $\tilde{\rho}_{\text{Max}}$ towards $\tilde{\rho}=0$.

3.1. Finite-grid representation

An alternative approach to solving the FPEs relies on representing the functions parametrizing the effective average action in a finite-dimensional space. Such a discretization recasts the ordinary differential equations into a large set of algebraic equations that can be solved with various methods e.g. the Newton–Raphson method. There are many ways in which such a finite-dimensional representation can be implemented, see e.g. [7, 14] employing Chebyshev polynomials for that purpose. In this work, however, we will study a more common and straightforward approach based on the grid representation.

Let us consider a $N_\rho+1$-point uniformly-spaced grid $\{\tilde{\rho}_i = i\,h_\rho\}_{i\in\overline{0,N_\rho}}$ spanning an interval $[0,\tilde{\rho}_{\text{Max}}]$ with $\tilde{\rho}_{\text{Max}} = h_\rho N_\rho$. Subsequently, let us reduce the domain of each parametrizing function f to the discrete set of grid points $\{\tilde{\rho}_i = i\,h_\rho\}$, thus reducing f to a vector of values $(f(\tilde{\rho}_0),\ldots,\tilde{f}(\tilde{\rho}_{N_\rho}))$. In a grid representation, the $\tilde{\rho}$ derivatives cannot be calculated analytically and have to be approximated with finite differences.

There are several different ways of constructing finite-difference approximations for the derivatives. In this work, we adopt a simple scheme, in which the derivative at the point $\tilde{\rho}_i$ is approximated by a linear combination of function values at n grid points closest to $\tilde{\rho}_i$ for n equal 3, 5, 7, or 9. The coefficients defining a linear combination approximating the dth derivative $f^{(d)}(\tilde{\rho}_i)$ can be derived directly from the Taylor expansion, see [32]. For $n>d$, there is a unique set of coefficients defining an approximation of $f^{(d)}(\tilde{\rho}_i)$ accurate up to corrections of order $O\left(h_\rho^{n-d}\right)$[3]. In this scheme, the discrete derivative operators D_n^d can be represented with matrices acting on the vectors of function values. E.g. for $N_\rho=4$, the three-point discrete derivative operators take the form:

---

[3] In some cases, when a central derivative formula is employed the approximation can be of the order $O\left(h_\rho^{n-d+1}\right)$ due to symmetry.

$$D_3^1 f = \frac{1}{h_\rho}\begin{pmatrix} -\frac{3}{2} & 2 & -\frac{1}{2} & 0 & 0 \\ -\frac{1}{2} & 0 & \frac{1}{2} & 0 & 0 \\ 0 & -\frac{1}{2} & 0 & \frac{1}{2} & 0 \\ 0 & 0 & -\frac{1}{2} & 0 & \frac{1}{2} \\ 0 & 0 & \frac{1}{2} & -2 & \frac{3}{2} \end{pmatrix}\begin{pmatrix} f\left(\tilde\rho_0\right) \\ f\left(\tilde\rho_1\right) \\ f\left(\tilde\rho_2\right) \\ f\left(\tilde\rho_3\right) \\ f\left(\tilde\rho_4\right) \end{pmatrix} = \begin{pmatrix} f^{(1)}\left(\tilde\rho_0\right) \\ f^{(1)}\left(\tilde\rho_1\right) \\ f^{(1)}\left(\tilde\rho_2\right) \\ f^{(1)}\left(\tilde\rho_3\right) \\ f^{(1)}\left(\tilde\rho_4\right) \end{pmatrix} + O\left(h_\rho^2\right), \tag{13a}$$

$$D_3^2 f = \frac{1}{h_\rho^2}\begin{pmatrix} 1 & -2 & 1 & 0 & 0 \\ 1 & -2 & 1 & 0 & 0 \\ 0 & 1 & -2 & 1 & 0 \\ 0 & 0 & 1 & -2 & 1 \\ 0 & 0 & 1 & -2 & 1 \end{pmatrix}\begin{pmatrix} f\left(\tilde\rho_0\right) \\ f\left(\tilde\rho_1\right) \\ f\left(\tilde\rho_2\right) \\ f\left(\tilde\rho_3\right) \\ f\left(\tilde\rho_4\right) \end{pmatrix} = \begin{pmatrix} f^{(2)}\left(\tilde\rho_0\right) \\ f^{(2)}\left(\tilde\rho_1\right) \\ f^{(2)}\left(\tilde\rho_2\right) \\ f^{(2)}\left(\tilde\rho_3\right) \\ f^{(2)}\left(\tilde\rho_4\right) \end{pmatrix} + \begin{pmatrix} O\left(h_\rho\right) \\ O\left(h_\rho^2\right) \\ O\left(h_\rho^2\right) \\ O\left(h_\rho^2\right) \\ O\left(h_\rho\right) \end{pmatrix}. \tag{13b}$$

Higher-order discrete derivative operators employed in our calculations are presented in appendix B. Note that the corrections to the second-derivative approximation are of order $O(h_\rho^2)$ in bulk, but only $O(h_\rho)$ at the borders. Higher accuracy of the bulk approximation arises due to the symmetry of the expressions which cannot be achieved at the border. Interestingly, we will see that the convergence rate for the estimates of the critical exponents is determined by the order of the corrections for the bulk approximation rather than the border expressions.

In the finite-grid representation, the FPEs form a set of algebraic equations treating each grid-point value of each parametrizing function as an independent variable. This system of equations can be relatively easily solved with standard numerical methods; the Newton–Raphson method is a particularly efficient tool for this purpose. We note that the Newton–Raphson method requires an initial guess for the FP solution which is improved in an iterative procedure. We have found, that to find the critical FP in the three-dimensional $O(N)$ models it is often sufficient to adopt the initial guess with the 'Mexican-hat' type potential and constant kinetic terms:

$$\tilde U\left(\tilde\rho\right) = \frac{\tilde u}{2}\left(\tilde\rho - \tilde\rho_0\right)^2, \; \tilde Z_\sigma\left(\tilde\rho\right) = \tilde Z_\pi\left(\tilde\rho\right) = 1, \tag{14}$$

for some constants $\tilde u$ and $\tilde\rho_0$. We also note that this scheme is easily generalized to more complex settings. It has been recently implemented both at higher orders of the DE [4, 5], as well as, for calculations involving more than one invariant [33–35].

3.2. Method of lines (MOL)

Let us recall equation (11) describing the flow of an infinitesimal perturbation $\{\epsilon f_V(t,\tilde\rho), \epsilon f_{Z_\sigma}(t,\tilde\rho), \epsilon f_{Z_\pi}(t,\tilde\rho)\}$ around the FP $\mathcal{F}^*$:

$$\partial_t \begin{pmatrix} f_V\left(t,\tilde\rho\right) \\ f_{Z_\sigma}\left(t,\tilde\rho\right) \\ f_{Z_\pi}\left(t,\tilde\rho\right) \end{pmatrix} = \mathcal{M}\left(\tilde\rho\right)\begin{pmatrix} f_V\left(t,\tilde\rho\right) \\ f_{Z_\sigma}\left(t,\tilde\rho\right) \\ f_{Z_\pi}\left(t,\tilde\rho\right) \end{pmatrix} \tag{15}$$

with $\mathcal{M}(\tilde{\rho})$ denoting a second-order differential operator called the stability operator. Linear partial differential equations such as equation (15) can be solved via the so-called MOL. In this approach, the $\tilde{\rho}$ space is discretized and, consequently, the stability operator $\mathcal{M}(\tilde{\rho})$ is approximated by a finite-dimensional stability matrix M. Subsequently, the problem is either integrated numerically as an initial value problem or the spectrum $\{\lambda_i, F_i\}$ of M is resolved to calculate time dependence analytically.

In the RG context, we are seldom interested in actual solutions to equation (15). Oftentimes, we only want to obtain the eigenvalues of the stability operator $\mathcal{M}$ which are connected to the critical exponents. Nevertheless, we can draw important insights from the MOL. In particular, we note the well-known issue with the MOL that while several leading eigenvalues of M offer a good approximation of the leading eigenvalues of $\mathcal{M}$ the accuracy quickly degrades for subsequent eigenvalues [36, 37]. As discussed in section 4, our calculations confirm this prediction. For a detailed review of the MOL, see [38].

Since, in our approach, the FP solution is already calculated in a discretized form, it is natural to use the same grid representation for the stability matrix. Let $\mathcal{F}_{a\tilde{\rho}_i}$ denote the value of the parametrizing function a at the grid point $\tilde{\rho}_i$. The entries of the stability matrix are defined as:

$$M_{a\tilde{\rho}_i, b\tilde{\rho}_j} := \left.\frac{\partial\left(\partial_t \mathcal{F}_{a\tilde{\rho}_i}\right)}{\partial \mathcal{F}_{b\tilde{\rho}_j}}\right|_{\mathcal{F}=\mathcal{F}^*}. \tag{16}$$

Calculating the stability matrix one has to mind that the anomalous dimension is not an independent variable and the terms of the form

$$\left.\frac{\partial\left(\partial_t \mathcal{F}_{a\tilde{\rho}_i}\right)}{\partial \eta}\frac{\partial \eta}{\partial \mathcal{F}_{b\tilde{\rho}_j}}\right|_{\mathcal{F}=\mathcal{F}^*} \tag{17}$$

also contribute to $M_{a\tilde{\rho}_i, b\tilde{\rho}_j}$. We also note that the value $\tilde{Z}_\pi(\tilde{\rho}_\eta) = 1$ is fixed and, consequently, the row $M_{\tilde{Z}_\pi \tilde{\rho}_\eta, b\tilde{\rho}_j}$ and the column $M_{b\tilde{\rho}_j, \tilde{Z}_\pi \tilde{\rho}_\eta}$ should be removed from the matrix[4]. Finally, analyticity of the effective action requires $\tilde{Z}_\sigma(0) = \tilde{Z}_\pi(0)$ and therefore the values $\tilde{Z}_\sigma(0)$ and $\tilde{Z}_\pi(0)$ should be treated as a single parameter.

The derivatives in equation (16) can be calculated either analytically or numerically. Calculating the derivatives analytically can be very effective when implementing the DE in a symbolic environment like *Mathematica*. This approach avoids approximation errors and can sometimes be more computationally efficient than the finite-difference approach. Beyond the order $O(\partial^2)$, however, the FPEs become incredibly complex and calculating the stability matrix in a symbolic framework becomes essentially infeasible. In a non-symbolic setting (e.g. in *C++* or *Fortran*), calculating the derivatives analytically is a tedious task that, to our knowledge, has never been performed. In this case, it is common and significantly more convenient to approximate the derivatives with finite differences.

---

[4] There are implementations of this scheme in which one does consider the perturbation of $\tilde{Z}_\pi(\tilde{\rho}_\eta)$. This, however, introduces a redundant operator connected to an approximately zero eigenvalue, thus drastically increasing the condition number of M and reducing the numerical accuracy when resolving its spectrum.

https://doi.org/10.1088/1742-5468/ad6c31

Like in the case of $\tilde{\rho}$ derivatives, the derivation of the finite-difference approximation is based on the Taylor expansion. The three lowest-order central approximations for the first derivative read:

$$\begin{aligned} f'(x) &= \frac{3}{4\epsilon}\left(f(x+\epsilon)-f(x-\epsilon)\right)-\frac{3}{20\epsilon}\left(f(x+2\epsilon)-f(x-2\epsilon)\right) \\ &\quad +\frac{1}{60\epsilon}\left(f(x+3\epsilon)-f(x-3\epsilon)\right)+O\left(\epsilon^6\right) \\ &= \frac{2}{3\epsilon}\left(f(x+\epsilon)-f(x-\epsilon)\right)-\frac{1}{12\epsilon}\left(f(x+2\epsilon)-f(x-2\epsilon)\right)+O\left(\epsilon^4\right) \\ &= \frac{1}{2\epsilon}\left(f(x+\epsilon)-f(x-\epsilon)\right)+O\left(\epsilon^2\right). \end{aligned} \tag{18}$$

We calculate the column $M_{\cdot\cdot,b\tilde{\rho}_j}$ of the stability matrix by perturbing the function b of the FP action at the point $\tilde{\rho}_j$ by a multiple of a small parameter ϵ. Subsequently, we calculate the time derivative of each perturbed action and combine them using one of the formulas (18) to obtain the column of the stability matrix. It is important to note that unlike in the $\tilde{\rho}$ space in this functional space, we do not introduce any grid representation. As a consequence, there are no boundary expressions like in equation (13), and the small parameter ϵ can be freely tuned to maximize the numerical precision.

In our calculations, we compute the derivatives defining the stability matrix analytically. The only exception is presented in figures 8 and 9 where we investigate the precision of the finite-difference approximation for the stability matrix.

3.3. Loop integrals

The loop integrals appearing in the fRG β functions (see equation (5)) can be performed analytically only for a specially selected IR regulators. Unless such a regulator is employed, the integrals have to be approximated numerically. In the fRG literature, there are several methods commonly utilized for performing these integrals including the Simpson's rule and various Gaussian quadratures. In the present work, we perform integrals analytically at the LPA level when the Litim regulator is used and employ the Gauss–Legendre quadrature otherwise. Unless specified otherwise, we perform the Gauss–Legendre integral on the interval $|\boldsymbol{q}| \in [0,5]$ with 35 evaluation points ensuring that the integration error does not exceed 10^{-10} in any β function at any grid point. For a detailed description of Gaussian quadrature rules, see to [36].

For the investigated models, the integrals are single-loop d-dimensional spherically symmetric integrals. It is typical, to integrate out the spherical component analytically and reduce the integral to a one-dimensional integral with respect to $q=|\boldsymbol{q}|$ or $y=\boldsymbol{q}^2$.[5] In the case of three-dimensional models, the latter choice introduces a square-root-like nonanalyticity to the integrand around $y=0$. This is inconvenient from the perspective of numerical integration since most numerical integration techniques offer

---

[5] In the β functions in [22], we include a constant $v_d=\frac{1}{2^{d+1}\pi^d\Gamma(d/2)}$ which absorbs the angular-integration constant as well as the factor $\frac{1}{(2\pi)^d}$ (see equation (5)). In the calculations, however, we set $v_d=1$; this can be understood as the rescaling $\tilde{\rho}\to\tilde{\rho}/v_d$, $\Gamma\to\Gamma/v_d$, which does not affect the physical quantities. To avoid confusion regarding the rescaling convention we always measure $\tilde{\rho}_{\mathrm{Max}}$ and h_ρ in the units of the minimum of the fixed-point local potential $\tilde{\rho}_0$.

error bounds involving derivatives of the integrand, e.g. for the Simpson's 3/8 rule the error bound is proportional to the fourth derivative of the integrand at some point within the integration domain. Due to a nonanalyticity introduced by the choice of y as the integration variable, the error bounds become very large and the convergence of the integral approximation becomes very slow. For this reason, we choose to integrate with respect to $q = |\boldsymbol{q}|$. Although it is not directly relevant to this study, we note that in non-integer dimensions, the issue of nonanalyticity cannot be easily circumvented by a better choice of integration variable and has to be dealt with in some other way.

3.4. Floating-point arithmetic

In numerical calculations, real numbers are typically stored as binary numbers with a fixed finite number of digits. As a consequence, most real numbers cannot be represented exactly and are rounded when represented as a floating-point number thus introducing rounding errors. As we show in section 4, rounding errors are a relevant concern for high-precision calculations. Although in our calculations we use the *Mathematica* software which allows for storing real numbers with arbitrary precision, we perform most of our calculations in a '64-bit double' format (represented by 'MachinePrecision' in *Mathematica*) offering a precision of approximately 16 decimal digits. This way we simulate the results that could be obtained if the same procedures were programmed in a low-level language like *C++* or *Fortran*. In some cases, to establish the reference values for exponents with higher precision we use an extended floating-point precision similar to (but not equivalent to) '80-bit double' or 'long double' format.

4. Numerical error propagation

We identify five categories of numerical errors that we want to investigate:

- compactification errors—the errors associated with representing the parametrizing functions on the compact interval $\tilde{\rho} \in [0, \tilde{\rho}_{\mathrm{Max}}]$ rather than the entire non-negative real semiaxis;
- discretization errors—the errors connected to representing the parametrizing functions on a discrete grid;
- integration errors—the errors induced by performing the loop integrals numerically;
- stability-matrix-approximation errors—the errors coming from the finite-difference approximation of the derivatives defining the stability matrix;
- rounding errors—the errors of the floating-point arithmetic.

In this chapter, we present several analyses that quantify the effect of each of these errors on the precision of several leading RG eigenvalues e_i and the anomalous dimension η. In these analyses, we isolate specific categories of errors by examining how the precision of the critical exponents depends on various numerical parameters. For this purpose, we will often assume that some errors are uncorrelated, e.g. that the integration error is not impacted by a change in the grid spacing h_ρ. With this assumption in mind, for each analysis, we identify a reference value e^{ref} for a critical exponent e, with respect to which

https://doi.org/10.1088/1742-5468/ad6c31

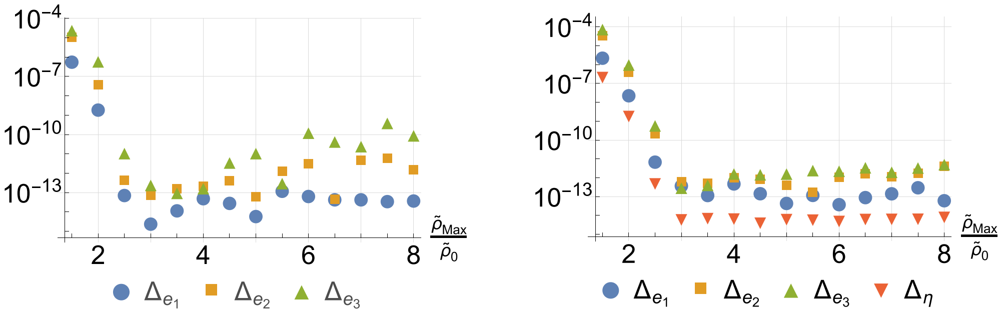

(a) Results at the LPA level.

(b) Results at the order $O(\partial^2)$.

Figure 1. Precision of the critical exponents as a function of $\tilde{\rho}_{\mathrm{Max}}$ for $h_\rho = \tilde{\rho}_0/20$. The reference values for each exponent were calculated for $\tilde{\rho}_{\mathrm{Max}} = 3.5\tilde{\rho}_0$ with the extended floating-point precision.

the numerical error is measured. The reference value is calculated with a significantly reduced error of the categories investigated in a given analysis. We emphasize, however, that this reference value is burdened by the other, uncorrelated kinds of numerical error.

All the results presented in this chapter were obtained for the three-dimensional $O(2)$ model. We performed analogous calculations for the $O(1)$ and $O(3)$ models and reached the same conclusions. For transparency, the results for these two models are presented in the repository in [22]. The details of numerical methods used for each of the analyses are summarized in appendix A.

4.1. Compactification error

Firstly, we investigate the error associated with restricting the parametrizing functions' domain to a compact set. We achieve that by tracking the critical exponents' errors with varying $\tilde{\rho}_{\mathrm{Max}}$ while keeping $h_\rho = \tilde{\rho}_0/20$ fixed [$\tilde{\rho}_0$ denotes the minimum of the local potential]. This way, we separate the discretization error, controlled primarily by h_ρ, from the compactification error. In this calculation, specifying the reference values, with respect to which the errors are measured, is a challenging task because by increasing $\tilde{\rho}_{\mathrm{Max}}$ we also increase the number of points, which might induce other kinds of errors, e.g. associated with the rising condition number of the stability matrix. The reference values were calculated with the extended floating-point precision with $\tilde{\rho}_{\mathrm{Max}} = 3.5\tilde{\rho}_0$. The coefficient 3.5 was determined phenomenologically as the value for which the errors were minimized.

The results of this analysis at the LPA and $O(\partial^2)$ orders of the DE are presented in figure 1 as a function of $\tilde{\rho}_{\mathrm{Max}}$. In both cases, the compactification error is relatively large at $\tilde{\rho}_{\mathrm{Max}} = 1.5\tilde{\rho}_0$ and drops precipitously with increasing $\tilde{\rho}_{\mathrm{Max}}$ reaching a plateau at $\tilde{\rho}_{\mathrm{Max}} \approx 3.5\tilde{\rho}_0$. Beyond this value, a slight difference between the two cases arises. At the LPA level, the plateau is very narrow and we can observe a slow deterioration of precision for large $\tilde{\rho}_{\mathrm{Max}}$. At the order $O(\partial^2)$, no significant deterioration is observed and the plateau continues until $\tilde{\rho}_{\mathrm{Max}} = 8\tilde{\rho}_0$.

https://doi.org/10.1088/1742-5468/ad6c31

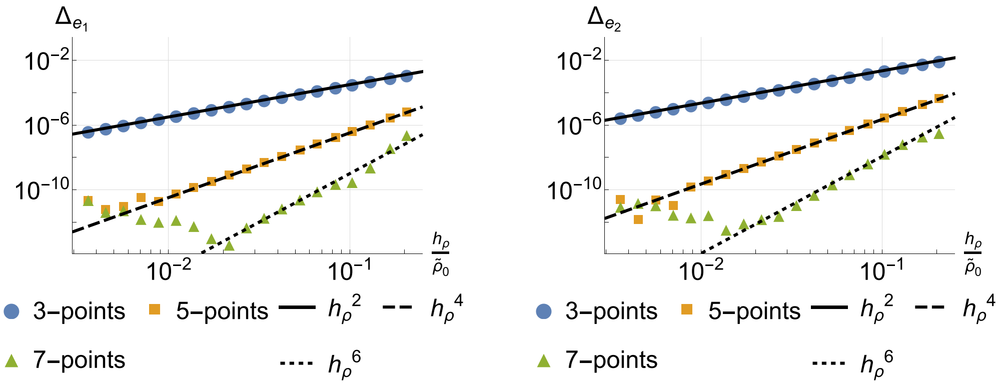

(a) Leading eigenvalue e_1. (b) Subleading eigenvalue e_2.

Figure 2. Precision of the critical exponents as a function of h_ρ for $\tilde\rho_{\text{Max}} = 3.5\tilde\rho_0$ at the LPA level. The reference values for each exponent were calculated with 9-point derivative approximation for $\tilde h_\rho = \tilde\rho_0/40$ with the extended floating-point precision. Lines represent the best power-law fits to several trailing points with integer exponents.

4.2. Discretization error

The primary parameter controlling the discretization error is the grid spacing h_ρ. Assuming the linear error propagation and disregarding the reduced accuracy of the derivative approximation at the borders, the error associated with discretization should be of order $O(h_\rho^{n-1})$ when the n-point approximation is employed. To verify the linear error propagation we track the error of the critical exponents as a function of the grid spacing using the 3-, 5-, and 7-point derivative approximation. The reference values for this analysis are calculated using the 9-point derivative approximation with the extended floating-point precision for $h_\rho = \tilde\rho_0/40$.

In figure 2, we track the exponents' dependence on the grid spacing h_ρ at the LPA level for $\tilde\rho_{\text{Max}} = 3.5\tilde\rho_0$—the optimal value established in the previous analysis. All the data series, in the figure, tend to 0 with $h_\rho \to 0$. This means that the estimates for the critical exponents converge to the same reference values irrespective of the discretization scheme. Moreover, the convergence rates are the same as the exponents controlling the corrections of the (bulk) finite-difference approximation for $\tilde\rho$ derivatives. For the seven-point approximation, we can also observe the rounding errors overtake the discretization errors around $h_\rho \approx 0.02\tilde\rho_0$. For lower values of h_ρ, the rounding errors lead to a slow decrease in accuracy. Essentially identical conclusions can be drawn from figure 3 presenting the results of analogous analysis at the order $O(\partial^2)$. This shows that, when properly set up, the discretization scheme employed in our calculations is convergent and can offer great accuracy.

We also performed an analysis similar to the one described above but with a significantly lower value of $\tilde\rho_{\text{Max}} = 2\tilde\rho_0$. Its results are presented in figures 4 and 5 for the LPA and $O(\partial^2)$ orders respectively. The overall precision and the convergence rates are significantly worse when compared to the results obtained for the optimal value of $\tilde\rho_{\text{Max}}$. More worryingly, instead of converging towards 0, all data series in both figures display

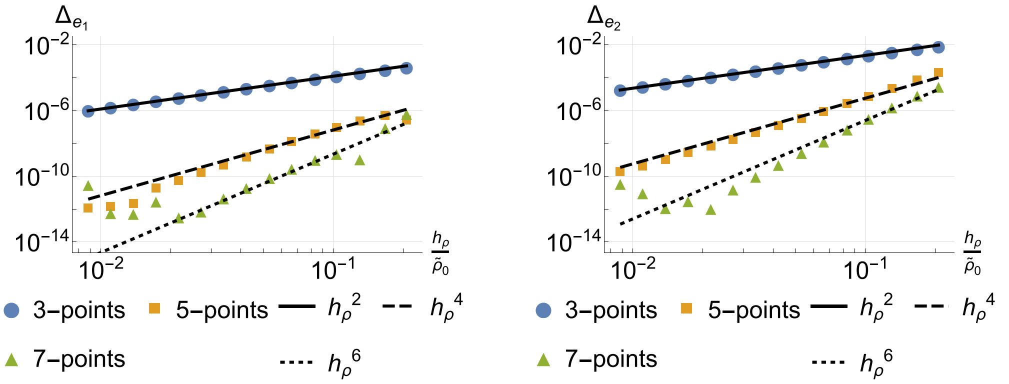

(a) Leading eigenvalue e_1.

(b) Subleading eigenvalue e_2.

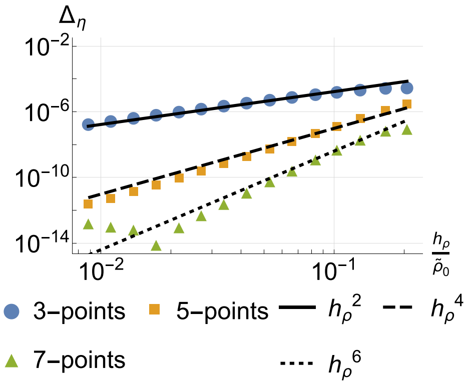

(c) Anomalous dimension η.

Figure 3. Precision of the critical exponents as a function of h_ρ for $\tilde{\rho}_{\mathrm{Max}} = 3.5\tilde{\rho}_0$ at the $O(\partial^2)$ order of the DE. The reference values for each exponent were calculated with nine-point derivative approximation for $\tilde{h}_\rho = \tilde{\rho}_0/40$ with the extended floating-point precision. Lines represent the best power-law fits to several trailing points with integer exponents.

a plateau for a wide range of values of h_ρ. This implies that neither of the discretization schemes converges to the reference value. We verified that for each exponent each data series converges to a different value. This analysis showcases that the error induced by selecting a too small a value of $\tilde{\rho}_{\mathrm{Max}}$ observed in figure 1 is primarily caused by an impaired convergence of the discretization scheme.

Finally, we compare the discretization accuracy between subsequent RG eigenvalues. Figure 6 shows the dependence of the eigenvalue error Δ_{e_i} on the eigenvalue index i (sorted in descending order with respect to the real part). At both the LPA and the $O(\partial^2)$ orders of the DE, we can see an exponential decay of precision with each subsequent eigenvalue. This observation is particularly pertinent for studies of multicritical points where we are often interested in more than a few leading eigenvalues.

In the figure, we marked a distinction between real and complex eigenvalues. We note that the stability matrix is real and non-symmetric so it can feature pairs of mutually conjugate complex eigenvalues. In the figure, such pairs have been reduced to a single point. Notably, complex eigenvalues are observed only at the $O(\partial^2)$ order of the DE and

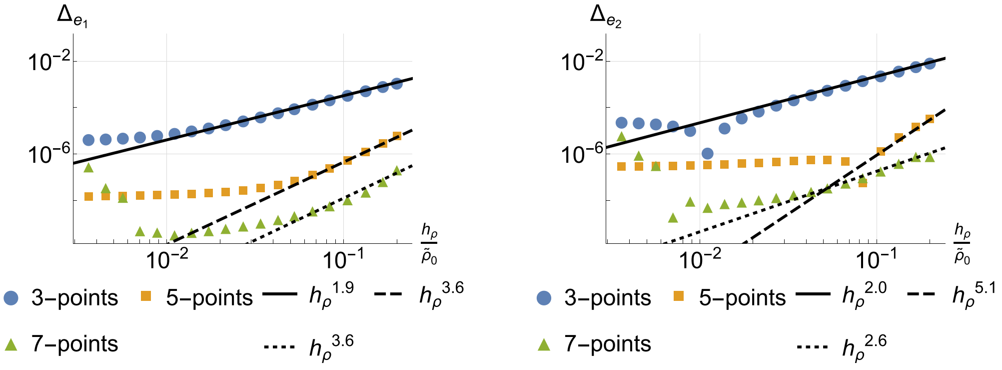

(a) Leading eigenvalue e_1. (b) Subleading eigenvalue e_2.

Figure 4. Precision of the critical exponents as a function of h_ρ for $\tilde\rho_{\mathrm{Max}} = 2\tilde\rho_0$ at the LPA level. The reference values for each exponent were calculated with nine-point derivative approximation for $\tilde h_\rho = \tilde\rho_0/40$ with the extended floating-point precision. Lines represent the best power-law fits to several trailing points.

their precision is typically lower than that of similar real eigenvalues by approximately one order of magnitude. The origin and physical meaning of the complex eigenvalues are not well understood and require future clarification.

4.3. Integration error

Let us now turn our attention to the numerical integration error. To be precise, we are not interested in the question of how to achieve a specific level of precision of numerical integrals. The answer to this question will be specific both to the investigated model and to the employed method. We ask the more general question about how the integration error propagates to errors in estimates of the critical exponents. To answer this question we calculate the critical exponents with progressively improving integral accuracy. On the technical level, we achieve this by performing the loop integrals with the Gauss–Legendre quadrature on the interval $|\boldsymbol{q}| \in [0, 5.5]$ with the number of evaluation points n varying between 5 and 40. For each value n, we define the integral error as:

$$\Delta_I(n) = \max_{a,\tilde\rho_i} |\tilde\beta_a^n(\tilde\rho_i) - \tilde\beta_a^{50}(\tilde\rho_i)|. \tag{19}$$

In the definition above, the maximum is taken over all parametrizing functions a and all grid points $\tilde\rho_i$, $\tilde\beta_a^n$ denotes the dimensionless β function for the function a calculated with n-point integral approximation, and $\tilde\beta_a^{50}$ serves as a reference value. The β functions in the definition (19) were evaluated at the fRG FP solution obtained with $\tilde\rho_{\mathrm{Max}} = 3.5\tilde\rho_0$, $h_\rho = \tilde\rho_0/20$ and 50-point integral approximation. Since the Litim regulator allows for analytical integration at the LPA level, it would be pointless to investigate the integration error in this setting. Therefore, in this analysis, we employ the exponential regulator both at the LPA and $O(\partial^2)$ orders.

In figure 7, we chart the precision of the critical exponents against the precision of the loop integrals. The figure clearly shows that the two errors are directly proportional.

J. Stat. Mech. (2024) 093204

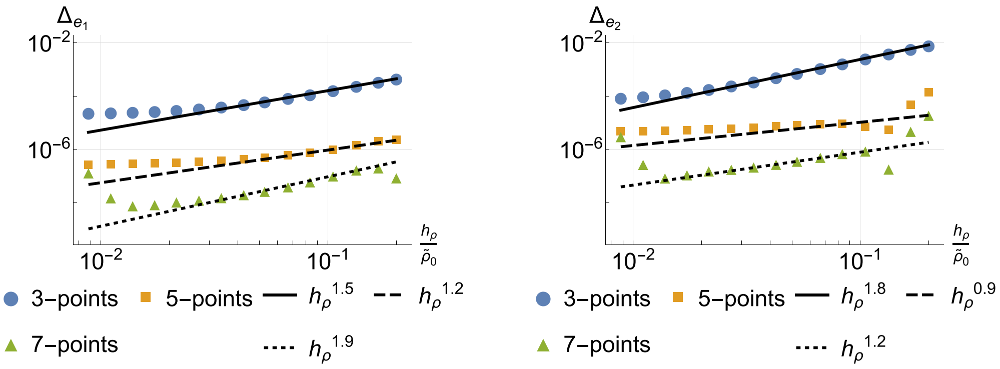

(a) Leading eigenvalue e_1. (b) Subleading eigenvalue e_2.

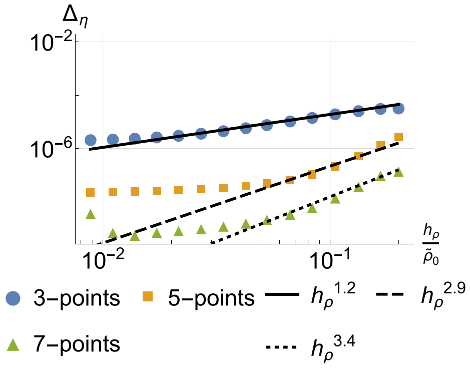

(c) Anomalous dimension η.

Figure 5. Precision of the critical exponents as a function of h_ρ for $\tilde{\rho}_{\text{Max}} = 2\tilde{\rho}_0$ at the order $O(\partial^2)$. The reference values for each exponent were calculated with nine-point derivative approximation for $\tilde{h}_\rho = \tilde{\rho}_0/40$ with the extended floating-point precision. Lines represent the best power-law fits to several trailing points.

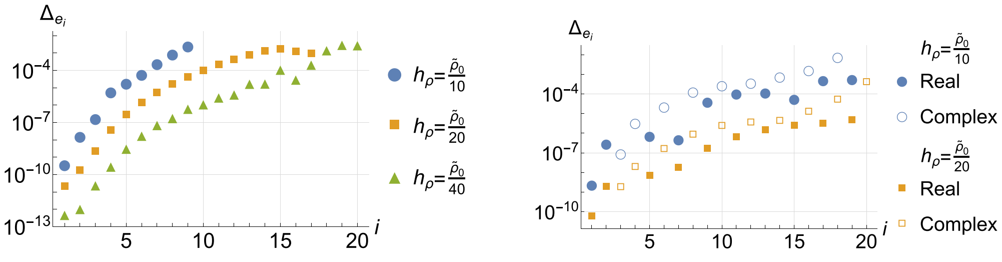

(a) Results at the LPA level. (b) Results at the order $O(\partial^2)$.

Figure 6. Dependence of the eigenvalue error Δ_{e_i} on the eigenvalue index i (sorted in descending order with respect to the real part) calculated for $\tilde{\rho}_{\text{Max}} = 3.5\tilde{\rho}_0$ with different values of grid spacing h_ρ. The reference values for each exponent were calculated with the extended floating-point precision for $h_\rho = \tilde{\rho}_0/60$ at the LPA level and $h_\rho = \tilde{\rho}_0/30$ at the order $O(\partial^2)$ using seven-point derivative approximation.

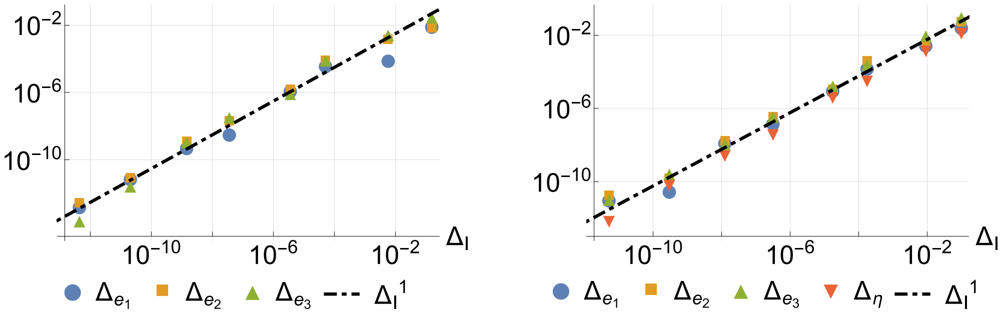

(a) Results at the LPA level.

(b) Results at the order $O(\partial^2)$.

Figure 7. Precision of the critical exponents as a function of integral precision Δ_I. The lines denote the best linear fit to several trailing points. In the calculation, we employed the seven-point approximation for the $\tilde{\rho}$ derivatives with $\tilde{\rho}_{\text{Max}} = 3.5\tilde{\rho}_0$ and $h_\rho = \tilde{\rho}_0/20$.

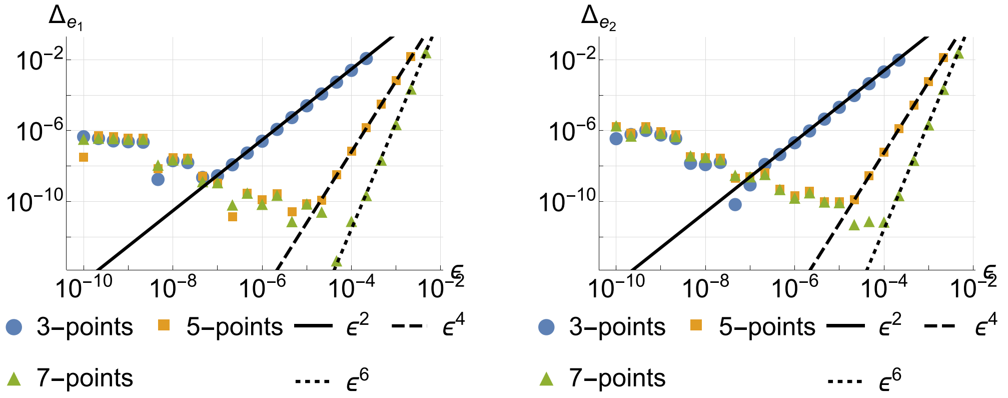

(a) Leading eigenvalue e_1.

(b) Subleading eigenvalue e_2.

Figure 8. Precision of the two leading RG eigenvalues as a function of the perturbation ϵ used in the stability-matrix finite-difference approximation calculated at the LPA level. Lines represent the best power-law fits to several trailing points with integer exponents. In the calculation, we employed the seven-point approximation for the $\tilde{\rho}$ derivatives with $\tilde{\rho}_{\text{Max}} = 3.5\tilde{\rho}_0$ and $h_\rho = \tilde{\rho}_0/20$. The reference values were extracted from the analytically constructed stability matrix.

Moreover, the errors of the critical exponents are of the same order of magnitude as the integration errors Δ_I. This means that, when implementing the numerical procedures for the loop integral, we do not need to test their accuracy on the critical exponents which would require a significant numerical effort; it is sufficient to test their accuracy directly on the β functions.

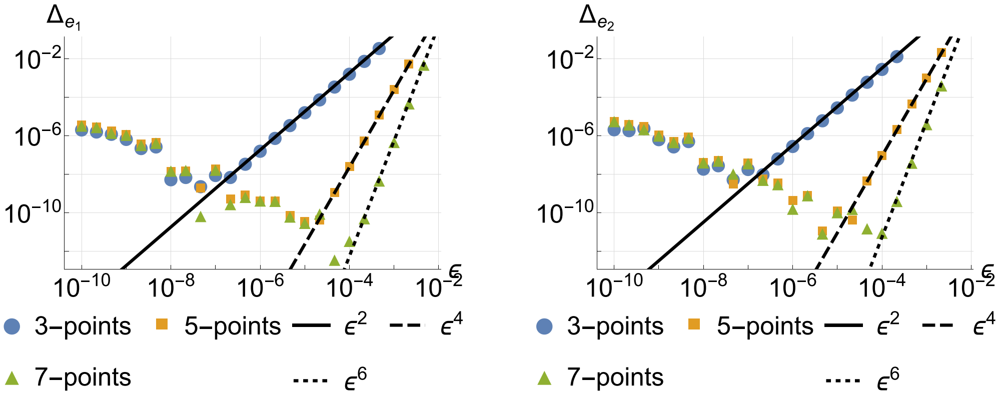

(a) Leading eigenvalue e_1.

(b) Subleading eigenvalue e_2.

Figure 9. Precision of the two leading RG eigenvalues as a function of the perturbation ϵ used in the stability-matrix finite-difference approximation calculated at the order $O(\partial^2)$. Calculation were performed with $\tilde{\rho}_{\mathrm{Max}} = 3.5\tilde{\rho}_0$ and $h_\rho = \tilde{\rho}_0/20$. The reference values were extracted from the analytically constructed stability matrix. Lines represent the best power-law fits to several trailing points with integer exponents.

4.4. Stability matrix approximation error

Finally, we examine the finite-difference approximation of the stability matrix. We calculate the eigenvalues of the stability matrix constructed with 3-, 5-, and 7-point approximations (see equation (18)) for a wide range of values for the perturbation parameter ϵ and compare them to the eigenvalues of analytically calculated stability matrix.

Figure 8 presents the results of this analysis at the LPA level. For large values of ϵ, we observe that the approximation is convergent with the expected rate of $n-1$ for n-point approximation. For small enough ϵ, each approximation breaks down as the rounding errors overtake the finite-difference-approximation errors. Interestingly, for all three approximations, the rounding errors all follow the exact same line $\sim \epsilon^{-1}$ with just a few random outliers [6]. Figure 9 shows the results of analogous calculation at the order $O(\partial^2)$. Remarkably, the results for two orders of the DE are almost identical.

5. Conclusion

In this work, we investigated the numerical accuracy of the stability-matrix approach to the fRG. We thoroughly examined the common numerical implementation of this scheme and identified major sources of numerical errors. Subsequently, we performed several tests to quantify the magnitude of these errors and verify the convergence of our numerical scheme.

---

[6] The outliers can be expected, as sometimes despite the rounding error the approximate value can randomly land close to the exact value. Importantly, there are no outliers above the ϵ^{-1} line.

Our calculations clearly show that the stability-matrix approach with the grid representation is a robust scheme allowing for remarkably precise calculations. Performing the calculations in the 64-bit floating-point representation we can calculate the five leading RG eigenvalues with the numerical error smaller than 10^{-8}, the value far below the typical error of the DE at this order lying between 10^{-2} and 10^{-4} [5]. We emphasize, that such accuracy can only be achieved when all the parameters of the numerical implementation are properly tuned.

Interestingly, the numerical errors obtained at the order $O(\partial^2)$ are essentially identical to those calculated at the LPA level, despite a three-times difference in the number of parameters and a wide difference in complexity of the β functions. We can, thus, reasonably expect that the order of magnitude of the numerical errors characterizing higher orders of the DE should remain roughly the same. We stress that, if needed, the numerical errors can be reduced even further by adopting a more precise floating-point representation.

Most of the calculations presented in this work, show that the employed numerical schemes converge with the theoretically predicted convergence rate. There is, however, one important exception to this rule. Selecting too small a value for the upper bound of the $\tilde{\rho}$ grid $\tilde{\rho}_{\mathrm{Max}}$ strongly impairs the convergence with respect to the grid spacing h_ρ. We have shown that imposing $\tilde{\rho}_{\mathrm{Max}} < 3.5\tilde{\rho}_0$ leads to a significant deterioration of the numerical accuracy. We note that increasing $\tilde{\rho}_{\mathrm{Max}}$ beyond $3.5\tilde{\rho}_0$ (with fixed h_ρ) has essentially no effect on the accuracy but quickly increases the numerical burden.

We emphasize that all calculations for this work were performed in the relatively simple three-dimensional $O(N)$ models. While we can expect the general conclusions to hold more broadly, specific error estimates should be recalculated for each case. The rounding errors are particularly strongly implementation-dependent and have to be carefully assessed. We suggest the methods presented in this work as a convenient tool for benchmarking the accuracy of numerical implementations of the fRG and tuning the values of numerical parameters.

Acknowledgments

We are grateful to Paweł Jakubczyk for the discussions as well as for reading the early version of the manuscript and very useful comments. We thank Carlos A Sanchéz Villalobos for his useful comments on the early version of the manuscript.

We acknowledge funding from the Polish National Science Center via Grant 2017/26/E/ST3/00211 and from the University of Warsaw via IDUB Programme, Action IV.4.1. *A complex programme of support for UW PhD students.*

Appendix A. Details of numerical calculations

Table A1. Numerical parameters of all calculations performed in this study. $\tilde{\rho}_{\mathrm{Max}}$ denotes the upper bound of the $\tilde{\rho}$ grid, and h_ρ denotes the grid spacing. DA stands for the $\tilde{\rho}$ derivative approximation, IR—for the loop integration range (with respect to $q = |\boldsymbol{q}|$), GL—for the Gauss–Legendre quadrature, SM—for the method of calculating the derivatives defining the stability matrix, and FPP - for the floating-point precision.

Calculation	DE order	$\tilde{\rho}_{\mathrm{Max}}$	h_ρ	DA	IR	Integral	SM	FPP
Compactification error (figure 1(a)) Reference value	LPA	Varied $3.5\tilde{\rho}_0$	$\tilde{\rho}_0/20$	7-point	$[0,1]$	Analytical	Analytical	64-bit double 80-bit double
Compactification error (figure 1(b)) Reference value	$O(\partial^2)$	Varied $3.5\tilde{\rho}_0$	$\tilde{\rho}_0/20$	7-point	$[0,5]$	35-point GL	Analytical	64-bit double 80-bit double
Discretization error (figure 2) Reference value	LPA	$3.5\tilde{\rho}_0$	Varied $\tilde{\rho}_0/40$	Varied 9-point	$[0,1]$	Analytical	Analytical	64-bit double 80-bit double
Discretization error (figure 3) Reference value	$O(\partial^2)$	$3.5\tilde{\rho}_0$	Varied $\tilde{\rho}_0/40$	Varied 9-point	$[0,5]$	35-point GL	Analytical	64-bit double 80-bit double

(Continued.)

https://doi.org/10.1088/1742-5468/ad6c31

Table A1. (Continued.)

Calculation	DE order	$\tilde{\rho}_{\mathrm{Max}}$	h_ρ	DA	IR	Integral	SM	FPP
Discretization error (figure 4) Reference value	LPA	$2\tilde{\rho}_0$	Varied $\tilde{\rho}_0/40$	Varied 9-point	$[0,1]$	Analytical	Analytical	64-bit double 80-bit double
Discretization error (figure 5) Reference value	$O(\partial^2)$	$2\tilde{\rho}_0$	Varied $\tilde{\rho}_0/40$	Varied 9-point	$[0,5]$	35-point GL	Analytical	64-bit double 80-bit double
Discretization error (figure 6(a)) Reference values	LPA	$3.5\tilde{\rho}_0$	Varied $\tilde{\rho}_0/60$	7-point	$[0,1]$	Analytical	Analytical	64-bit double 80-bit double
Discretization error (figure 6(b)) Reference values	$O(\partial^2)$	$3.5\tilde{\rho}_0$	Varied $\tilde{\rho}_0/30$	7-point	$[0,5]$	35-point GL	Analytical	64-bit double 80-bit double
Integration error (figure 7) Reference values	LPA/$O(\partial^2)$	$3.5\tilde{\rho}_0$	$\tilde{\rho}_0/20$	7-point	$[0,5.5]$	Varied GL 50-point GL	Analytical	64-bit double 80-bit double
Stability-matrix error (figures 8) Reference values	LPA	$3.5\tilde{\rho}_0$	$\tilde{\rho}_0/20$	7-point	$[0,1]$	Analytical	Finite difference [Varied] Analytical	64-bit double
Stability-matrix error (figures 9) Reference values	$O(\partial^2)$	$3.5\tilde{\rho}_0$	$\tilde{\rho}_0/20$	7-point	$[0,5]$	35-point GL	Finite difference [Varied] Analytical	64-bit double

Appendix B. Discrete derivative operators

In section 3, we discussed the finite-difference approximations for derivatives in the $\tilde{\rho}$-discretization scheme and provided expressions for the 3-point discrete derivative operators D^1_3 and D^2_3 approximating $\partial_{\tilde{\rho}}$ and $\partial^2_{\tilde{\rho}}$ operators respectively. Below, we present the five-point operators D^1_5 and D^2_5 for $N_\rho = 6$, the seven-point operators D^1_7 and D^2_7 for $N_\rho = 8$, and the nine-point operators D^1_9 and D^2_9 for $N_\rho = 10$:

$$D^1_5 = \frac{1}{h_\rho}\begin{pmatrix} -\frac{25}{12} & 4 & -3 & \frac{4}{3} & -\frac{1}{4} & 0 & 0 \\ -\frac{1}{4} & -\frac{5}{6} & \frac{3}{2} & -\frac{1}{2} & \frac{1}{12} & 0 & 0 \\ \frac{1}{12} & -\frac{2}{3} & 0 & \frac{2}{3} & -\frac{1}{12} & 0 & 0 \\ 0 & \frac{1}{12} & -\frac{2}{3} & 0 & \frac{2}{3} & -\frac{1}{12} & 0 \\ 0 & 0 & \frac{1}{12} & -\frac{2}{3} & 0 & \frac{2}{3} & -\frac{1}{12} \\ 0 & 0 & -\frac{1}{12} & \frac{1}{2} & -\frac{3}{2} & \frac{5}{6} & \frac{1}{4} \\ 0 & 0 & \frac{1}{4} & -\frac{4}{3} & 3 & -4 & \frac{25}{12} \end{pmatrix}, \tag{B.1a}$$

$$D^2_5 = \frac{1}{h^2_\rho}\begin{pmatrix} \frac{35}{12} & -\frac{26}{3} & \frac{19}{2} & -\frac{14}{3} & \frac{11}{12} & 0 & 0 \\ \frac{11}{12} & -\frac{5}{3} & \frac{1}{2} & \frac{1}{3} & -\frac{1}{12} & 0 & 0 \\ -\frac{1}{12} & \frac{4}{3} & -\frac{5}{2} & \frac{4}{3} & -\frac{1}{12} & 0 & 0 \\ 0 & -\frac{1}{12} & \frac{4}{3} & -\frac{5}{2} & \frac{4}{3} & -\frac{1}{12} & 0 \\ 0 & 0 & -\frac{1}{12} & \frac{4}{3} & -\frac{5}{2} & \frac{4}{3} & -\frac{1}{12} \\ 0 & 0 & -\frac{1}{12} & \frac{1}{3} & \frac{1}{2} & -\frac{5}{3} & \frac{11}{12} \\ 0 & 0 & \frac{11}{12} & -\frac{14}{3} & \frac{19}{2} & -\frac{26}{3} & \frac{35}{12} \end{pmatrix}, \tag{B.1b}$$

$$D^1_7 = \frac{1}{h_\rho}\begin{pmatrix} -\frac{49}{20} & 6 & -\frac{15}{2} & \frac{20}{3} & -\frac{15}{4} & \frac{6}{5} & -\frac{1}{6} & 0 & 0 \\ -\frac{1}{6} & -\frac{77}{60} & \frac{5}{2} & -\frac{5}{3} & \frac{5}{6} & -\frac{1}{4} & \frac{1}{30} & 0 & 0 \\ \frac{1}{30} & -\frac{2}{5} & -\frac{7}{12} & \frac{4}{3} & -\frac{1}{2} & \frac{2}{15} & -\frac{1}{60} & 0 & 0 \\ -\frac{1}{60} & \frac{3}{20} & -\frac{3}{4} & 0 & \frac{3}{4} & -\frac{3}{20} & \frac{1}{60} & 0 & 0 \\ 0 & -\frac{1}{60} & \frac{3}{20} & -\frac{3}{4} & 0 & \frac{3}{4} & -\frac{3}{20} & \frac{1}{60} & 0 \\ 0 & 0 & -\frac{1}{60} & \frac{3}{20} & -\frac{3}{4} & 0 & \frac{3}{4} & -\frac{3}{20} & \frac{1}{60} \\ 0 & 0 & \frac{1}{60} & -\frac{2}{15} & \frac{1}{2} & -\frac{4}{3} & \frac{7}{12} & \frac{2}{5} & -\frac{1}{30} \\ 0 & 0 & -\frac{1}{30} & \frac{1}{4} & -\frac{5}{6} & \frac{5}{3} & -\frac{5}{2} & \frac{77}{60} & \frac{1}{6} \\ 0 & 0 & \frac{1}{6} & -\frac{6}{5} & \frac{15}{4} & -\frac{20}{3} & \frac{15}{2} & -6 & \frac{49}{20} \end{pmatrix}, \tag{B.1c}$$

$$D_7^2 = \frac{1}{h_\rho^2}\begin{pmatrix}
\frac{203}{45} & -\frac{87}{5} & \frac{117}{4} & -\frac{254}{9} & \frac{33}{2} & -\frac{27}{5} & \frac{137}{180} & 0 & 0 \\
\frac{137}{180} & -\frac{49}{60} & -\frac{17}{12} & \frac{47}{18} & -\frac{19}{12} & \frac{31}{60} & -\frac{13}{180} & 0 & 0 \\
-\frac{13}{180} & \frac{19}{15} & -\frac{7}{3} & \frac{10}{9} & \frac{1}{12} & -\frac{1}{15} & \frac{1}{90} & 0 & 0 \\
\frac{1}{90} & -\frac{3}{20} & \frac{3}{2} & -\frac{49}{18} & \frac{3}{2} & -\frac{3}{20} & \frac{1}{90} & 0 & 0 \\
0 & \frac{1}{90} & -\frac{3}{20} & \frac{3}{2} & -\frac{49}{18} & \frac{3}{2} & -\frac{3}{20} & \frac{1}{90} & 0 \\
0 & 0 & \frac{1}{90} & -\frac{3}{20} & \frac{3}{2} & -\frac{49}{18} & \frac{3}{2} & -\frac{3}{20} & \frac{1}{90} \\
0 & 0 & \frac{1}{90} & -\frac{1}{15} & \frac{1}{12} & \frac{10}{9} & -\frac{7}{3} & \frac{19}{15} & -\frac{13}{180} \\
0 & 0 & -\frac{13}{180} & \frac{31}{60} & -\frac{19}{12} & \frac{47}{18} & -\frac{17}{12} & -\frac{49}{60} & \frac{137}{180} \\
0 & 0 & \frac{137}{180} & -\frac{27}{5} & \frac{33}{2} & -\frac{254}{9} & \frac{117}{4} & -\frac{87}{5} & \frac{203}{45}
\end{pmatrix}, \tag{B.1d}$$

$$D_9^1 = \begin{pmatrix}
-\frac{761}{280} & 8 & -14 & \frac{56}{3} & -\frac{35}{2} & \frac{56}{5} & -\frac{14}{3} & \frac{8}{7} & -\frac{1}{8} & 0 & 0 \\
-\frac{1}{8} & -\frac{223}{140} & \frac{7}{2} & -\frac{7}{2} & \frac{35}{12} & -\frac{7}{4} & \frac{7}{10} & -\frac{1}{6} & \frac{1}{56} & 0 & 0 \\
\frac{1}{56} & -\frac{2}{7} & -\frac{19}{20} & 2 & -\frac{5}{4} & \frac{2}{3} & -\frac{1}{4} & \frac{2}{35} & -\frac{1}{168} & 0 & 0 \\
-\frac{1}{168} & \frac{1}{14} & -\frac{1}{2} & -\frac{9}{20} & \frac{5}{4} & -\frac{1}{2} & \frac{1}{6} & -\frac{1}{28} & \frac{1}{280} & 0 & 0 \\
\frac{1}{280} & -\frac{4}{105} & \frac{1}{5} & -\frac{4}{5} & 0 & \frac{4}{5} & -\frac{1}{5} & \frac{4}{105} & -\frac{1}{280} & 0 & 0 \\
0 & \frac{1}{280} & -\frac{4}{105} & \frac{1}{5} & -\frac{4}{5} & 0 & \frac{4}{5} & -\frac{1}{5} & \frac{4}{105} & -\frac{1}{280} & 0 \\
0 & 0 & \frac{1}{280} & -\frac{4}{105} & \frac{1}{5} & -\frac{4}{5} & 0 & \frac{4}{5} & -\frac{1}{5} & \frac{4}{105} & -\frac{1}{280} \\
0 & 0 & -\frac{1}{280} & \frac{1}{28} & -\frac{1}{6} & \frac{1}{2} & -\frac{5}{4} & \frac{9}{20} & \frac{1}{2} & -\frac{1}{14} & \frac{1}{168} \\
0 & 0 & \frac{1}{168} & -\frac{2}{35} & \frac{1}{4} & -\frac{2}{3} & \frac{5}{4} & -2 & \frac{19}{20} & \frac{2}{7} & -\frac{1}{56} \\
0 & 0 & -\frac{1}{56} & \frac{1}{6} & -\frac{7}{10} & \frac{7}{4} & -\frac{35}{12} & \frac{7}{2} & -\frac{7}{2} & \frac{223}{140} & \frac{1}{8} \\
0 & 0 & \frac{1}{8} & -\frac{8}{7} & \frac{14}{3} & -\frac{56}{5} & \frac{35}{2} & -\frac{56}{3} & 14 & -8 & \frac{761}{280}
\end{pmatrix}, \tag{B.1e}$$

$$D_9^2 = \frac{1}{h_\rho^2}\begin{pmatrix}
\frac{29531}{5040} & -\frac{962}{35} & \frac{621}{10} & -\frac{4006}{45} & \frac{691}{8} & -\frac{282}{5} & \frac{2143}{90} & -\frac{206}{35} & \frac{363}{560} & 0 & 0 \\
\frac{363}{560} & \frac{8}{315} & -\frac{83}{20} & \frac{153}{20} & -\frac{529}{72} & \frac{47}{10} & -\frac{39}{20} & \frac{599}{1260} & -\frac{29}{560} & 0 & 0 \\
-\frac{29}{560} & \frac{39}{35} & -\frac{331}{180} & \frac{1}{5} & \frac{9}{8} & -\frac{37}{45} & \frac{7}{20} & -\frac{3}{35} & \frac{47}{5040} & 0 & 0 \\
\frac{47}{5040} & -\frac{19}{140} & \frac{29}{20} & -\frac{118}{45} & \frac{11}{8} & -\frac{1}{20} & -\frac{7}{180} & \frac{1}{70} & -\frac{1}{560} & 0 & 0 \\
-\frac{1}{560} & \frac{8}{315} & -\frac{1}{5} & \frac{8}{5} & -\frac{205}{72} & \frac{8}{5} & -\frac{1}{5} & \frac{8}{315} & -\frac{1}{560} & 0 & 0 \\
0 & -\frac{1}{560} & \frac{8}{315} & -\frac{1}{5} & \frac{8}{5} & -\frac{205}{72} & \frac{8}{5} & -\frac{1}{5} & \frac{8}{315} & -\frac{1}{560} & 0 \\
0 & 0 & -\frac{1}{560} & \frac{8}{315} & -\frac{1}{5} & \frac{8}{5} & -\frac{205}{72} & \frac{8}{5} & -\frac{1}{5} & \frac{8}{315} & -\frac{1}{560} \\
0 & 0 & -\frac{1}{560} & \frac{1}{70} & -\frac{7}{180} & -\frac{1}{20} & \frac{11}{8} & -\frac{118}{45} & \frac{29}{20} & -\frac{19}{140} & \frac{47}{5040} \\
0 & 0 & \frac{47}{5040} & -\frac{3}{35} & \frac{7}{20} & -\frac{37}{45} & \frac{9}{8} & \frac{1}{5} & -\frac{331}{180} & \frac{39}{35} & -\frac{29}{560} \\
0 & 0 & -\frac{29}{560} & \frac{599}{1260} & -\frac{39}{20} & \frac{47}{10} & -\frac{529}{72} & \frac{153}{20} & -\frac{83}{20} & \frac{8}{315} & \frac{363}{560} \\
0 & 0 & \frac{363}{560} & -\frac{206}{35} & \frac{2143}{90} & -\frac{282}{5} & \frac{691}{8} & -\frac{4006}{45} & \frac{621}{10} & -\frac{962}{35} & \frac{29531}{5040}
\end{pmatrix}. \tag{B.1f}$$

References

[1] Wetterich C 1993 Exact evolution equation for the effective potential *Phys. Lett.* B **301** 90–94

[2] Morris T R 1994 Derivative expansion of the exact renormalization group *Phys. Lett.* B **329** 241–8

[3] Morris T R 1997 Three-dimensional massive scalar field theory and the derivative expansion of the renormalization group *Nucl. Phys.* B **495** 477–504

[4] Balog I, Chaté H, Delamotte B, Marohnić M and Wschebor N 2019 Convergence of nonperturbative approximations to the renormalization group *Phys. Rev. Lett.* **123** 240604

[5] De Polsi G, Balog I, Tissier M and Wschebor N 2020 Precision calculation of critical exponents in the O(N) universality classes with the nonperturbative renormalization group *Phys. Rev.* E **101** 1–24

[6] Balog I, De Polsi G, Tissier M and Wschebor N 2020 Conformal invariance in the nonperturbative renormalization group: a rationale for choosing the regulator *Phys. Rev.* E **101** 062146

[7] Borchardt J and Knorr B 2016 Solving functional flow equations with pseudospectral methods *Phys. Rev.* D **94** 025027

[8] Aoki K I, Kumamoto S I and Yamada M 2018 Phase structure of NJL model with weak renormalization group *Nucl. Phys.* B **931** 105–31

[9] Grossi E, Ihssen F J, Pawlowski J M and Wink N 2021 Shocks and quark-meson scatterings at large density *Phys. Rev.* D **104** 016028

[10] Koenigstein A, Steil M J, Wink N, Grossi E, Braun J, Buballa M and Rischke D H 2022 Numerical fluid dynamics for FRG flow equations: zero-dimensional QFTs as numerical test cases. I. The O(N) model *Phys. Rev.* D **106** 065012

[11] Beyer J, Goth F and Müller T 2022 Better integrators for functional renormalization group calculations *Eur. Phys. J.* B **95** 116

[12] Ihssen F, Sattler F R and Wink N 2023 Numerical RG-time integration of the effective potential: analysis and benchmark *Phys. Rev.* D **107** 114009

[13] Ihssen F and Pawlowski J M 2023 Functional flows for complex effective actions *SciPost Phys.* **15** 074

[14] Borchardt J and Knorr B 2015 Global solutions of functional fixed point equations via pseudospectral methods *Phys. Rev.* D **91** 105011 Borchardt J and Knorr B 2016 Erratum: global solutions of functional fixed point equations via pseudospectral methods [Phys. Rev. D 91, 105011 (2015)] *Phys. Rev.* D **93** 089904

[15] Tan Y, Huang C, Chen Y and Fu W 2022 Criticality of the $O(N)$ universality via global solutions to nonperturbative fixed-point equations (arXiv:2211.10249)

[16] Wolfram Research Inc. 2023 *Mathematica, Version 13.3* (available at: www.wolfram.com/mathematica)

[17] Berges J, Tetradis N and Wetterich C 2002 Non-perturbative renormalization flow in quantum field theory and statistical physics *Phys. Rep.* **363** 223–386

[18] Kopietz P, Bartosch L and Schütz F 2010 Introduction to the Functional Renormalization Group *Phase Transitions Renorm. Gr* (Springer)

[19] Gies H 2012 *Introduction to the Functional RG and Applications to Gauge Theories* (*Lecture Notes in Physics* vol 852) ed A Schwenk and J Polonyi (Springer) pp 287–348

[20] Dupuis N, Canet L, Eichhorn A, Metzner W, Pawlowski J M, Tissier M and Wschebor N 2021 The nonperturbative functional renormalization group and its applications *Phys. Rep.* **910** 1–114

[21] Canet L, Delamotte B, Mouhanna D and Vidal J 2003 Optimization of the derivative expansion in the nonperturbative renormalization group *Phys. Rev.* D **67** 065004

[22] Chlebicki A (2024) *fRGNumericalPrecision* (available at: https://zenodo.org/records/11084865)

[23] Baldazzi A, Zinati R B A and Falls K 2022 Essential renormalisation group *SciPost Phys.* **13** 085

[24] Morris T R 1995 The derivative expansion of the renormalization group *Nucl. Phys.* B **42** 811–3

[25] Codello A 2012 Scaling solutions in a continuous dimension *J. Phys. A: Math. Theor.* **45** 465006

[26] Bervillier C, Boisseau B and Giacomini H 2008 Analytical approximation schemes for solving exact renormalization group equations. II Conformal mappings *Nucl. Phys.* B **801** 296–315

[27] Defenu N and Codello A 2018 Scaling solutions in the derivative expansion *Phys. Rev.* D **98** 016013

[28] Codello A and D'Odorico G 2013 O(N)−universality Classes and the Mermin–Wagner theorem *Phys. Rev. Lett.* **110** 141601

[29] Codello A, Defenu N and D'Odorico G 2015 Critical exponents of O(N) models in fractional dimensions *Phys. Rev.* D **91** 105003

[30] Yabunaka S and Delamotte B 2017 Surprises in $O(N)$ Models: nonperturbative fixed points, large N limits and multicriticality *Phys. Rev. Lett.* **119** 191602

[31] Yabunaka S and Delamotte B 2018 Why might the standard large N analysis fail in the O(N) model: the role of cusps in fixed point potentials *Phys. Rev. Lett.* **121** 231601

[32] Fornberg B 1988 Generation of finite difference formulas on arbitrarily spaced grids *Math. Comput.* **51** 699–706

[33] Tissier M and Tarjus G 2012 Nonperturbative functional renormalization group for random field models and related disordered systems. IV. Supersymmetry and its spontaneous breaking *Phys. Rev.* B **85** 104203

[34] Delamotte B, Dudka M, Mouhanna D and Yabunaka S 2016 Functional renormalization group approach to noncollinear magnets *Phys. Rev.* B **93** 064405

[35] Chlebicki A, Sánchez-Villalobos C A, Jakubczyk P and Wschebor N 2022 $\mathbb{Z}_4$-symmetric perturbations to the XY model from functional renormalization *Phys. Rev.* E **106** 064135

[36] Süli E and Mayers D F 2003 *An Introduction to Numerical Analysis* (Cambridge University Press) p 433

[37] Butcher J C 2016 *Numerical Methods for Ordinary Differential Equations* (Wiley)

[38] Schiesser W E and Griffiths G W 2009 *A Compendium of Partial Differential equation Models* (Cambridge University Press)